Colloidal Continuous Injection Synthesis Of Fluorescent MoX_2 (X = S, Se) Nanosheets as a First Step Toward Photonic Applications

Gabriele Pippia,[a] Anastasia Rousaki,[a] Matteo Barbone,[b, c] Jonas Billet,[a] Rosaria Brescia,[d] Anatolii Polovitsyn,[d] Beatriz Martín-García,[d] Mirko Prato, [d] Francesco De Boni, [d] Marko M. Petrić,[b, c] Amine Ben Mhenni,[b] Isabel Van Driessche,[a] Peter Vandenabeele,[a, e] Kai Müller,[b, c] Iwan Moreels[a]

[a]Ghent University, Department of Chemistry, Krijgslaan 281, 9000 Gent, Belgium

[b]Walter Schottky Institut and Department of Electrical and Computer Engineering, Technische Universität München, Am Coulombwall 4, D - 85748 Garching, Germany

[c]Munich Center for Quantum Science and Technology (MCQST), Schellingstrasse 4, 80799 Munich, Germany

[d]Istituto Italiano di Tecnologia, Via Morego 30, 16163 Genova, Italy

[e]Ghent University, Department of Archaeology, Sint-Pietersnieuwstraat 35, 9000 Gent, Belgium

KEYWORDS

Colloidal synthesis, transition metal dichalcogenide, design of experiments, molybdenum disulfide, molybdenum diselenide

ABSTRACT

Transition-metal dichalcogenide (TMD) nanosheets have become an intensively investigated topic in the field of 2D nanomaterials, especially due to the direct-semiconductor nature, and the broken inversion symmetry in odd-layer number, of some of their family members. These properties make TMDs attractive for different technological applications such as photovoltaics, optoelectronics, valleytronics, and hydrogen evolution reactions (HER). Among them, MoX_2 (X = S, Se) are turned to direct-gap when their thickness is thinned down to monolayer, thus, efforts towards obtaining large-scale monolayer TMDs are crucial for technological applications. Colloidal synthesis of TMDs has been developed in recent years as it provides a cost-efficient and scalable way to produce few-layer TMDs having homogeneous size and thickness, yet obtaining a monolayer has proven challenging. Here, we present a method for the colloidal synthesis of mono- and few-layer MoX_2 (X = S, Se) using elemental chalcogenide and metal chloride as precursors. Using a synthesis with slow injection of the $MoCl_5$ precursor under nitrogen atmosphere, and optimizing the synthesis parameters with a Design Of Experiments (DOE) approach, we obtained a MoX_2 sample with the semiconducting (1H) phase, optical band gaps of 1.96 eV for 1H-MoS_2 and 1.67 eV for 1H-$MoSe_2$, respectively, consistent with a large monolayer yield in the ensemble. Both display photoluminescence at cryogenic and room temperature, paving the way for optical spectroscopy studies and photonic applications of colloidal TMD nanosheets.

INTRODUCTION

Transition Metal Dichalcogenides (TMDs) are a class of materials formed of stacks of three-atom-thick single-layers with structure X-M-X and general formula MX_2 (M = transition metal, X = chalcogen), with separate layers held together by Van der Waals interactions. TMDs have electronic properties that span from insulators to semiconductors and semimetals.[1] Among them, molybdenum disulfide (MoS_2) can be prepared in three different polytypes, trigonal prismatic (2H, semiconducting, thermodynamically favoured), rhombohedral (3R, semiconducting, metastable)[2] or octahedral (1T, metallic, kinetically favoured).[3] Bulk 2H-MoS_2 is an indirect gap semiconductor with a band gap of 1.2 eV[4] that turns to a direct band gap of ~1.9 eV for a monolayer.[5] Molybdenum diselenide ($MoSe_2$) possesses similar properties, such as an indirect to direct band gap transition going from bulk to monolayer, with the gap increasing from 1.1 eV for bulk[4] to 1.6 eV for a monolayer,[6] a broken inversion symmetry[7-8] and the same 1T, 2H and 3R polytypes.[9] Such properties make this class intriguing for applications such as optoelectronics,[10] spintronics, vallytronics,[7, 11-12] and catalysis.[13-14] In addition, the flexible monolayer[15] allows for wearable devices.[10]

The weak nature of the Van der Waals interactions that bind the separate layers makes it possible to exfoliate TMDs using mechanical cleavage, in a similar fashion to that used by Novoselov *et al*. on graphite.[16] Over time, different exfoliation methods have been developed, such as liquid-phase exfoliation (LPE),[17] chemical exfoliation,[18] or laser thinning.[19] These methods can produce samples with low defect density and, depending on the method, have a good production rate (up to 1 $mg \cdot h^{-1}$).[20] However, they also produce polydisperse samples, containing TMDs with different thicknesses.[20] Therefore, at the same time efforts are made on bottom-up approaches to synthesize TMDs starting from molecular precursors. Chemical vapor deposition (CVD), hydro/solvothermal synthesis, colloidal synthesis are some of the methods that are used. Especially CVD provides materials nearly defect-free and a thickness down to a monolayer. In contrast, despite few examples,[21-27] colloidal synthesis at present does not provide TMD suspensions that are substantially free of multilayers.

In order to improve synthesis protocols, colloidal synthesis typically relies on the so-called One Variable At a Time (OVAT) approach, consisting of a loop optimization when all input factors (X_i) such as temperature, precursor concentration and reaction time, are held constant while one is varied until the best outcome (Y_i) is found. This optimization method, next to being time- and resource-consuming, is not able to give information on possible interactions between the input factors, nor does it consistently provide the optimal result. In this manuscript, we therefore replaced the OVAT approach by Design of Experiments (DOE), a statistical method used in fields such as engineering,[28] biology,[29] and recently chemistry[30-31] to speed up the optimization process and, different from OVAT, yields an overview on the role of the input factors involved in the synthesis. The main advantage of DOE is its ability to screen different factors at the same time, yielding information across the entire experimental domain, while OVAT typically provides a sparser sampling for the same number of experiments.[31] Via Design of Experiments, we obtained

a pathway towards a general method to produce monolayer MoS_2 and $MoSe_2$ TMD nanosheets with excellent monodispersity, beyond current state-of-the-art solution-based LPE,[32] with both MoS_2 and $MoSe_2$ exhibiting photoluminescence at both cryogenic and room temperatures, on par with LPE.[33]

RESULTS AND DISCUSSION

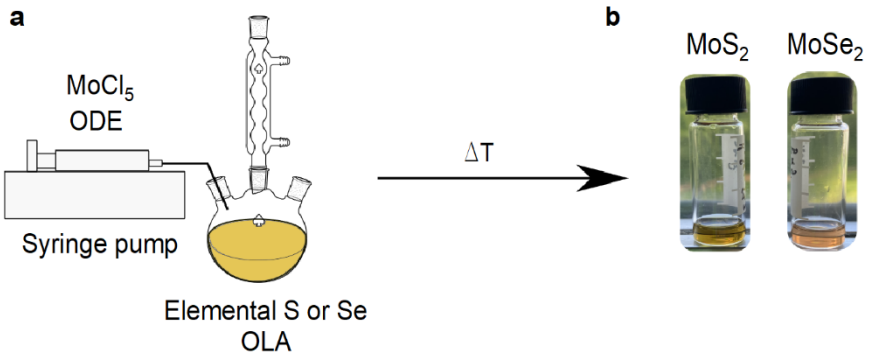

Scheme 1. (a) Scheme of the synthesis protocol used in this work. (b) Picture of MoS_2 and $MoSe_2$ samples dispersed in *o*-dichlorobenzene.

We use slow injection of a metal chloride solution in a hot solution of oleylamine (OLA) and elemental chalcogen under inert atmosphere (**Scheme 1**). OLA is a typical ligand used in colloidal synthesis of nanoparticles[34] and TMDs[35-36] as capping ligand and mild reducing agent.[34] A mixture of OLA and elemental sulfur can react with metal precursors leading to metal disulfide nanocrystals,[37] and a similar effect is reported for OLA and selenium mixtures.[38] A high reaction temperature is required to overcome the energy barrier of ~ 400 meV between the two phases,[39] and to achieve the 2H polytype.[14, 40-41]

Among the different DOE designs available, we use the Definitive Screening Design (DSD), developed in 2011 by Jones and Nachtsheim,[42] for DSD is capable of analysing the influence of different input factors within a predefined reaction space, using one of the fewest experimental runs.[43] Typically, with k the number of factors, one runs only $2k + 1$ experiments.[44] For this type of design, it is recommended to use a minimum of 6 factors (13 experiments), to avoid performance degradation.[43]

In our experiments, we kept the molybdenum precursor concentration, 1-octadecene (ODE) volume, and total reaction time constant. We chose to vary six input factors: reaction temperature, sulfur concentration, precursor injection rate, OLA volume, OLA degassing time, and OLA degassing temperature (**Table 1**). The first three were chosen as they may directly impact the nanosheet growth and final crystal phase.[14, 40-41] In addition, the amount of OLA may be linked to the colloidal stability in solution[45] and an *in situ* H_2S formation,[37] while the OLA degassing temperature and time are expected to influence the concentration of oxygen and water in the

reaction environment. The factor ranges (**Table 1**) used for DSD design were based on initial syntheses and available literature data.[20]

Table 1. Input factors X_i (i = [1,6]) used for the syntheses, and associated S/Mo molecular ratio. X_1: Reaction temperature, X_2: OLA volume, X_3: Sulfur concentration, X_4: Injection rate, X_5 degassing temperature, X_6: Degassing time.

Run no.	X_1 [°C]	X_2 [mL]	X_3 [mmol]	X_4 [mL·h^{-1}]	X_5 [°C]	X_6 [min]	S/Mo ratio
1	300	15	3.75	6	160	150	20.5
2	300	3	2.25	3	100	30	12.3
3	320	9	2.25	6	160	30	12.3
4	280	9	3.75	3	100	150	20.5
5	320	3	3	3	160	150	16.4
6	280	15	3	6	100	30	16.4
7	320	15	2.25	4.5	100	150	12.3
8	280	3	3.75	4.5	160	30	20.5
9	320	15	3.75	3	130	30	20.5
10	280	3	2.25	6	130	150	12.3
11	320	3	3.75	6	100	90	20.5
12	280	15	2.25	3	160	90	12.3
13	300	9	3	4.5	130	90	16.4

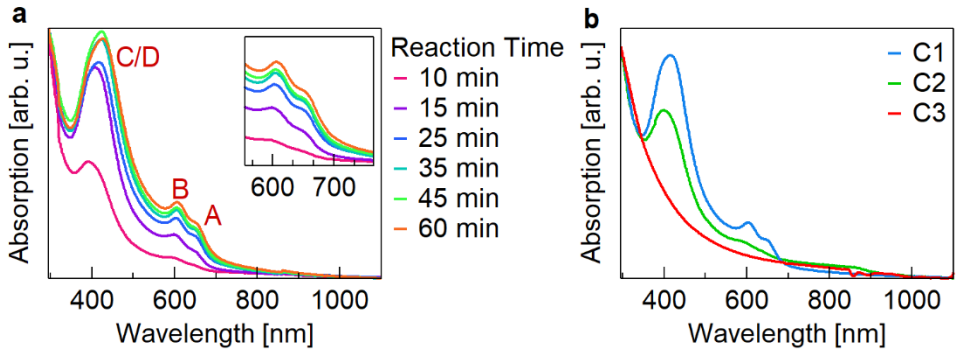

Figure 1. (a) Sample evolution during synthesis (synthesis run no. 1). Aliquots were taken between 10 and 60 min. A, B, and C/D mark the different features that can be observed when synthesizing 2H-MoS_2. Inset: zoom into the band gap region. (b) Representative absorption spectra of the three categories to which the DOE synthesis runs can be allocated. (C1: run no. 12, C2: run no. 10, C3: run no. 5). C1 corresponds to 2H-MoS_2, C2 to a mixture of 2H and 1T, and C3 to 1T MoS_2.

All samples are first characterized using UV-Vis spectroscopy. Analysis of the aliquots of a typical reaction (synthesis run no. 1) shows the appearance of three absorption (A, B and C/D) peaks after

10-15 min of reaction (**Figure 1a**), characteristic for the formation of semiconductor 2H-MoS_2 (for the evolution of sample C2 and C3 over time, see **Supporting Information, Figure S1**). The A and B exciton arise from the K point of the Brillouin zone while the C/D arise from transitions from a zone with parallel valence and conduction bands.[46] Longer reaction times lead to a progressive red shift (*i.e.* shift towards longer wavelength) of these features (**Figure 1a**). This shift is thickness and area-dependent.[27, 47] Initial inspection of the spectra of the final sample of all runs, taken after 60 min of reaction, shows that they can generally be categorized in three different sets, by the exciton peak sharpness: category C1 includes all samples when all the excitonic (A, B) transitions are well defined; category C2 contains the samples where only the C/D absorption peak is well defined, while C3 category includes all samples when no absorption features are recognizable (**Figure 1b,** and see **Supporting Information, Figure S2** for XPS characterization of sample C1 and C3). The absence is typical of 1T-MoS_2.[48] Hence, we can conclude that the synthesis parameters influence not only the nanosheet dimensions but also the crystal structure, where the 2H phase is obtained running the reaction at 300°C using a large excess of sulfur and OLA. Ideally, synthesized MoS_2 nanosheets are only a monolayer thick, of uniform dimensions, and with acceptable lateral sizes and dispersibility in the final solvent. These requirements are represented by a minimized wavelength for the A exciton absorption (due to the correlation between band gap energy and number of layers),[49-50] spectrally narrow absorption peaks (absorption peaks of different thicknesses overlap, yielding a broad peak as a result), and a low scattering background (large and/or aggregated nanosheets increase the scattering in the absorption spectrum),[51] respectively. We therefore decided to optimize these three responses Y_i (i = 1, 2, 3) of the final material. The scattering background is represented by the ratio of the absorbance at 750 nm and the absorbance at the position of the A exciton. The spectral position of the A exciton is calculated by second derivative analysis, after subtracting the scattering background from the spectra. For the absorption peak linewidth we use the ratio of the maximum peak absorbance at the spectral position of the B exciton transition and the absorbance at the following local minimum, which lies at slightly higher energy, as a proxy. We rely on the B exciton transition, as it is more pronounced that the A exciton transition (**Figure 1a**). For the DSD, we executed a total of 13 experiments, and for each run we collected seven aliquots to monitor the evolution of the samples over time (for the absorption spectrum of all the aliquots used in the DSD design see **Supporting Information, Figure S3**).

Table 2. Responses Y_i retrieved from the DOE experiments. Y_1: A exciton position, Y_2: Rayleigh scattering, Y_3: Absorption sharpness.

Run no.	Y_1 [nm]	Y_2	Y_3	Type
1	657	0.262	1.09	C1
2	665	0.608	0.91	C3
3	664	0.352	1.05	C1
4	654	0.350	1.01	C1

5	665	0.713	0.93	**C3**
6	652	0.418	1.00	**C2**
7	659	0.361	1.03	**C1**
8	650	0.579	0.95	**C3**
9	643	0.498	0.87	**C2**
10	642	0.568	0.93	**C2**
11	659	0.500	1.00	**C2**
12	653	0.228	1.11	**C1**
13	661	0.330	1.06	**C1**

A full overview of all responses Y_i is shown in **Table 2.** These responses are fitted to a quadratic surface, *i.e.* the fit considers both linear and quadratic dependencies on input factors, X_i, X_i^2, and $X_i \cdot X_j$. Importantly, the model yields a *p-value* for each input factor, *i.e.* an indication of the probability that the observed data comes from the null hypothesis, in this case that there is no correlation between the observed values and the factors. A threshold of 0.05 is typically chosen; if the *p-value* is below this threshold then the null hypothesis has to be rejected, *i.e.* there is no influence of the respective factor on the responses. For each Y_i, the model then finally yields an expression that predicts Y_i from the input factors (X_i, X_i^2, $X_i \cdot X_j$) that are statistically relevant.

Table 3. Coefficients and associated *p-values* of the main interaction factors, two-factors interactions and quadratic effects for A exciton position.

Factor		***p-value***
$\boldsymbol{X_1 \cdot X_2}$	Reaction T · OLA volume	0.00006
$\boldsymbol{X_1 \cdot X_3}$	Reaction T · Sulfur concentration	0.00010
$\boldsymbol{X_1}$	Reaction T	0.00022
$\boldsymbol{X_1^2}$	Reaction T · Reaction T	0.00052
$\boldsymbol{X_3}$	Sulfur concentration	0.00666
$\boldsymbol{X_2}$	OLA volume	0.01363

As an example, from the analysis of the A exciton position λ_A, six factors have been identified as statistically relevant: reaction temperature (X_1), OLA volume (X_2) and sulfur concentration (X_3), as well as the combinations, X_1^2, $X_1 \cdot X_2$ and $X_1 \cdot X_3$. The associated *p*-value of each factor is reported in **Table 3**. The modelling yields the following expression:

$$\lambda_A = 661 + 3.9 \cdot \left(\frac{(X1 - 300)}{20}\right) - 1.7 \cdot \left(\frac{(X2 - 9)}{6}\right) - 2 \cdot \left(\frac{(X3 - 3)}{0.75}\right) - 6.9 \cdot \left(\frac{(X1 - 300)}{20}\right)^2 - 5.667 \cdot \left(\frac{(X1 - 300)}{20}\right)\left(\frac{(X2 - 9)}{6}\right) - 5.167 \cdot \left(\frac{(X1 - 300)}{20}\right)\left(\frac{(X3 - 3)}{0.75}\right) \quad \textbf{(1)}$$

The expression can give some insights into the response of the A exciton position upon variation of the different input factors. An increase in reaction temperature leads to a red shift of the A exciton position, while an increase of the chalcogen and ligand concentrations results in a blue shift (*i.e.* a shift towards shorter wavelength). Hence, a reduced reaction temperature, in combination with high concentrations of OLA and chalcogen precursors are ideal conditions to obtain thin samples, with a blue shifted A exciton peak. At the same time, the precursor injection rate, OLA degassing time, and OLA degassing temperature have no significant impact on the peak position. The prediction expressions for the other two responses, the Rayleigh scattering background and peak sharpness, are reported in the **Supporting Information**.

The prediction of the model was then finally tested running a synthesis with parameters that are optimized toward a maximal blue shift of the A exciton position, a reduced Rayleigh scattering background, and sharp absorption features. The model proposed the following reaction conditions: a reaction temperature of 280 °C, OLA volume of 9 mL, sulfur concentration of 2.26 mmol, an OLA degassing time and temperature of 150 min at 160 °C, and a precursor injection rate of 6 $mL \cdot h^{-1}$. From this synthesis we acquired aliquots at the end of the reaction (60 min) and at the end of the injection of the Mo precursor (30 min). The experimental responses are compared to the predicted ones in **Table 4**.

Table 4. Comparison between predicted responses from DOE and experimental responses.

	A exciton position [nm]	**Rayleigh scattering parameter**	**Peak sharpness**
Predicted results	647 ± 1	0.49 ± 0.02	0.98 ± 0.03
Experimental results (30 min reaction)	653	0.40	1.03
Experimental results (60 min reaction)	654	0.50	0.95

First, we observe that the experimental value of the A exciton position is close to the predicted value. Note that this prediction was based on all values for the A exciton position, including those below 650 nm (see **Table 2**). In hindsight (*cfr.* below), these values (run no. 9 and run no. 10) show an A exciton position below the one expected even for a monolayer sample; however, during the DOE run we did not discriminate between values, yielding a slightly underestimated prediction compared to what can be obtained experimentally even for a monolayer. The Rayleigh scattering parameter prediction and peak sharpness are accurate for the 60 min aliquot. In conclusion, our model is able to predict the experimental conditions for which the thinnest possible MoS_2 nanosheet sample can be synthesized. Regarding the evolution of the sample during reaction, the A exciton peak position merely red shifts by 1 nm between 30 min and 60 min, indicating no

further growth in thickness after the end of the precursor injection. The Rayleigh scattering does further increase, suggesting a continued lateral growth of the nanosheets. This is accompanied by a decrease in peak sharpness.

This outcome was used as a basis to make a final improvement of Y_i, see methods for the final reaction conditions. We obtained a sample with A exciton absorption at 653 nm (**Figure 2a**), a Rayleigh scattering parameter of 0.35, and a peak sharpness of 1.06, indeed slightly improving on the previous sample (**Table 4**). The latter corresponds to a full width at half maximum (FWHM) of 36 nm. As LPE literature typically reports A exciton positions around 660 nm, pertaining to mixtures of different thicknesses,[52-54] we are clearly superseding the state-of-the-art in solution-based TMDs. We then proceeded to a further experimental study of the samples. High resolution transmission electron microscopy (HR-TEM) images of the sample were acquired to evaluate the crystal phase (**Figure 2b**). HRTEM and its fast Fourier Transform (FFT, **Figure 2c**) clearly confirms the 2H-MoS_2 semiconducting polytype phase, similar to what reported for samples obtained via LPE.[54]

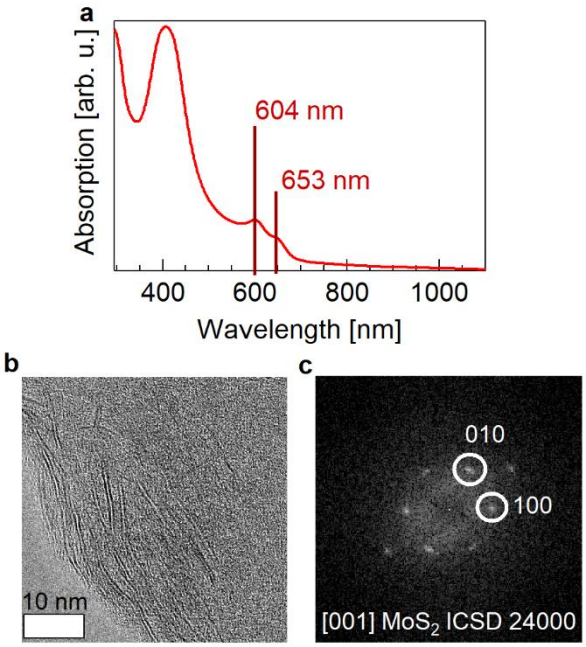

Figure 2. (a) UV-Vis absorption spectrum of MoS_2 nanosheets prepared *via* the optimized synthesis, including A and B exciton positions. (b) High Resolution TEM image of MoS_2. (c) FFT of the HRTEM image, indexed as [001]-oriented semiconducting MoS_2 (MoS_2-4H, ICSD 24000).

To assess the MoS_2 thickness, we used Raman spectroscopy (**Figure 3**). 2H-MoS_2 Raman spectra possess two first-order intralayer phonon modes, A_{1g} corresponding to the out-of-plane vibrational mode, and E^1_{2g} corresponding to the in-plane vibrational mode. They lie at 405.2 cm^{-1} and 384.5

cm^{-1} respectively (**Figure 3a**). The FWHM of the modes amounts to 5.5 cm^{-1} and 6.6 cm^{-1} for E^1_{2g} and A_{1g} respectively. In a highly crystalline sample these values are around 2.1 - 2.7 cm^{-1} and 3 cm^{-1} for E^1_{2g} and A_{1g} respectively.[55-56] A further broadening is usually observed in defective MoS_2.[57] Support for these defects can be observed via vibrational modes at 227 cm^{-1} and 996 cm^{-1}, related to sample disorder[57] or the presence of MoO_3, respectively.[58] In our case, the suppressed mode at 996 cm^{-1} suggest the presence of vacancies rather than MoO_3 (**Figure 3a**).[57]

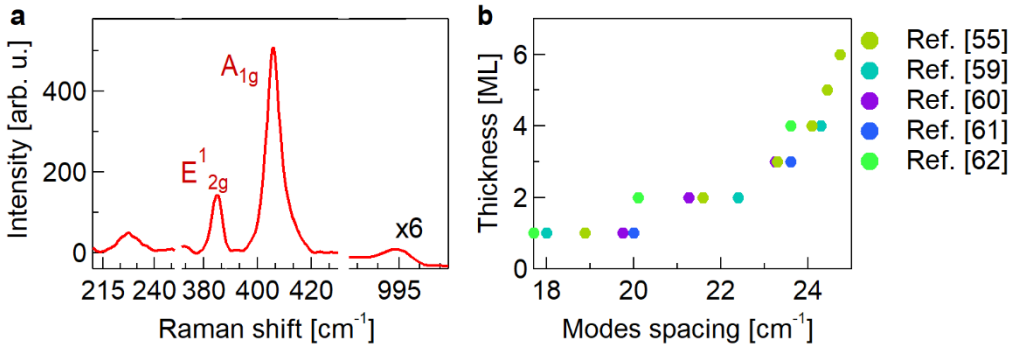

Figure 3. (a) Raman spectrum (excitation wavelength of 532 nm) of optimized MoS_2 sample, indicating E^1_{2g} and A_{1g} modes of colloidal 2H-MoS_2 at 405 cm^{-1} and 384 cm^{-1}. The mode at 227 cm^{-1} is associated to sample disorder, while a minor contribution from a MoO_x mode can be observed at 996 cm^{-1}.(b) Correlation between E^1_{2g} and A_{1g} mode spacing, and number of layers, using literature data.[55, 59-62]

Importantly, the E^1_{2g} and A_{1g} Raman modes are sensitive to the MoS_2 thickness. Literature data shows that, going from bulk to a monolayer, E^1_{2g} blue shifts (stiffens) while A_{1g} red shifts (softens), yielding a frequency spacing of 25 cm^{-1} for bulk that decreases to 21.3±1.2 cm^{-1} for a bilayer and 18.9±1.2 cm^{-1} for a monolayer (**Figure 3b**).[55, 59-62] The ranges for the mode spacing reported in literature prevents a quantitative assessment of number of layers present in our sample, however, from an average mode spacing (obtained from three different sample spots) of 20.8 ± 0.2 cm^{-1} of our optimized sample, we can estimate that we indeed synthesized a sample that consists at the most of a mixture of mono- and bilayer nanosheets. This is consistent with the A exciton position lying at 653 nm, which is close to the value of 650 nm reported in literature for a MoS_2 monolayer.[63]

To demonstrate the general applicability of our synthesis approach, the optimized protocol from the MoS_2 synthesis was further adapted to the synthesis of 2H-$MoSe_2$. In order to reduce the number of input factors involved, the degassing step involving OLA and chalcogen was removed, instead using distilled OLA stored over molecular sieves in a glovebox. Other factors of the protocol were kept the same, with only some adjustments of the precursor quantities (see **Methods**). The resulting nanosheets again possess two excitonic absorption peaks, here red shifted compared to MoS_2 due to the smaller $MoSe_2$ bandgap.

As shown by the TEM image (**Figure 4a**, inset), our $MoSe_2$ adopts a nanoflower morphology. HR-TEM images and their FFTs are compatible with trigonal prismatic $MoSe_2$ (**Figure 4b**), confirming the semiconducting phase.[64-65] The absorption spectrum (**Figure 4c**) shows the A and B exciton at 784 nm and 699 nm, with a FWHM of 66 nm and 50 nm respectively. As for the MoS_2, the $MoSe_2$ excitonic peaks are thickness-sensitive; literature reports a progressive blue shift of the A exciton absorption features, going from 815 nm in a 6 layer sample to 795 nm for a monolayer.[49] Our $MoSe_2$ sample shows an A exciton position slightly blue shifted compared to what is reported in literature for monolayer samples, indicating a monolayer thickness.

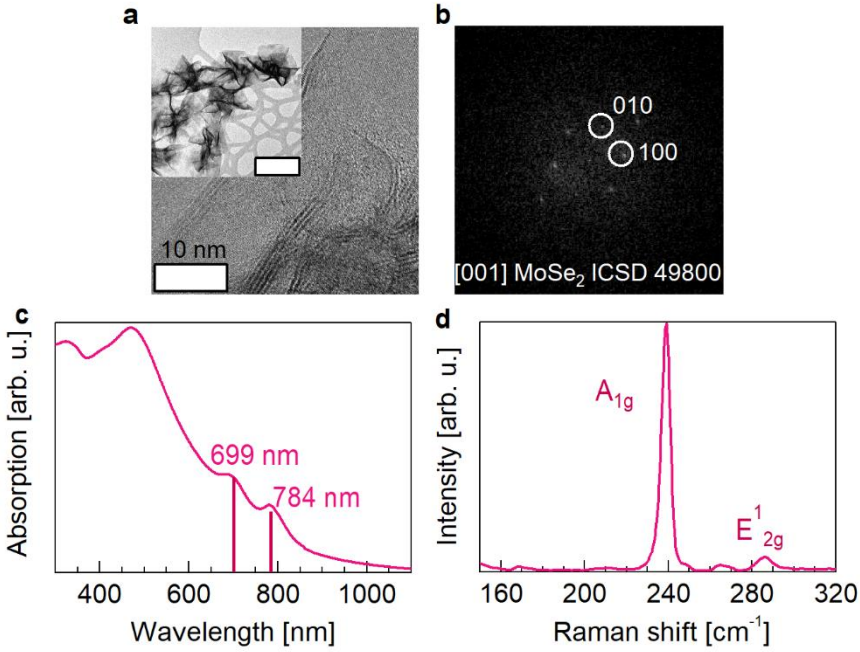

Figure 4. (a) HR-TEM image of the $MoSe_2$ sample, with the inset showing the nanoflower overall shape in a bright-field TEM image (scalebar: 100 nm). (b) FFT of the HRTEM image, indexed as a [001]-oriented hexagonal $MoSe_2$ ($MoSe_2$-4H, ICSD 49800). (c) UV-Vis absorption spectrum of colloidal 2H-$MoSe_2$, indicating the A and B exciton positions at 784 nm and 699 nm, respectively. (d) Raman spectrum of $MoSe_2$, showing two Raman modes A_{1g} and E^1_{2g}.

Similar to MoS_2, Raman spectroscopy can also be used to determine the number of layers in a $MoSe_2$ sample. While for MoS_2 the modes spacing is the benchmark to determine the thickness, for $MoSe_2$, both the modes position and the amplitude ratio of the Raman modes is thickness-dependent, with the amplitude ratio $I_{A_{1g}}/I_{E^1_{2g}}$ equal to 23.1 for a monolayer, reducing to 4.9 for a 10 layer sample, while the A_{1g} (E^1_{2g}) mode shifts from 243 cm^{-1} to 241 cm^{-1} (from 284 cm^{-1} to 287 cm^{-1}) going from bulk to a monolayer.[20, 66] Here, the E^1_{2g} and A_{1g} Raman modes (**Figure 4d**) are centered at 286 cm^{-1} and 239 cm^{-1}, respectively, with a amplitude ratio of 17.8 and an average mode spacing (obtained from three different spots) of 47.5 ± 0.8 cm^{-1}. Both the modes amplitude ratio, and modes position suggests that we are close to a monolayer thickness.[49]

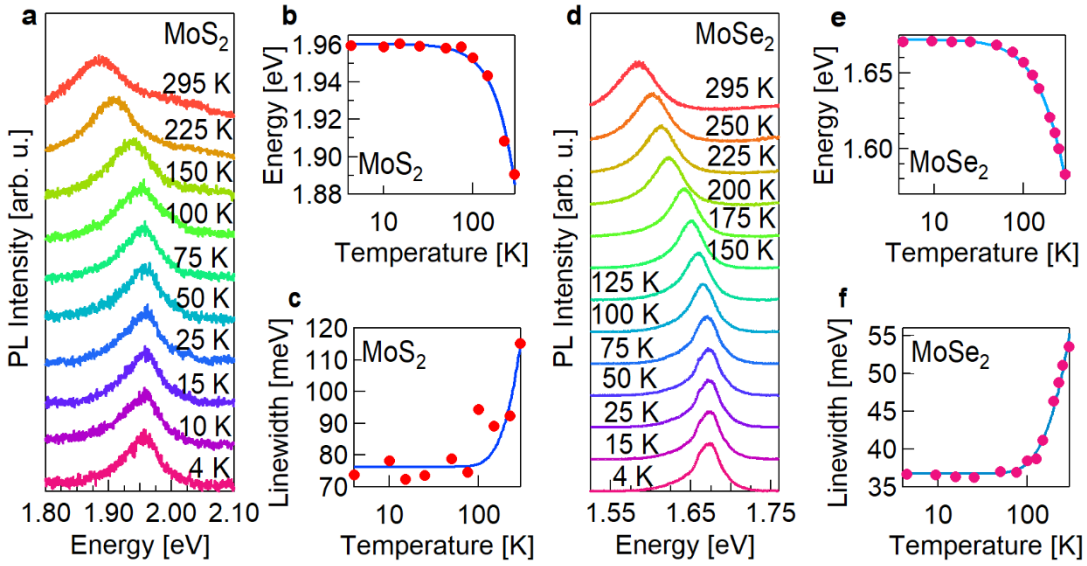

Figure 5. (a) Evolution of PL spectra of hBN encapsulated MoS_2 from 4 K to room temperature. (b) O'Donnell-Chen plot of hBN encapsulated MoS_2. (c) Evolution of emission linewidth with the temperature. (d) Evolution of PL spectra of hBN encapsulated $MoSe_2$ going from 4 K to room temperature. (e) O'Donnell-Chen plot of hBN encapsulated $MoSe_2$. (f) Evolution of emission linewidth with the temperature.

Finally, we investigated the photoluminescence properties of both samples. Fluorescent TMDs are usually obtained via mechanically exfoliated bulk crystals[67] or CVD,[68] however literature reports examples of fluorescent TMDs obtained via colloidal synthesis or LPE methods. Samples obtained via LPE method are usually able to show after extensive separation processes (to increase the monolayer fraction)[69] and different treatments such as annealing (used to restore the 2H phase)[40] or chemical treatments to suppress defects.[70] Literature reports about fluorescent colloidal TMDs includes pristine[71] and chemically treated colloidal WS_2 nanosheets,[72] as well as quantum dots (QDs).[73-76]

Samples with the highest optical quality require encapsulating mechanically cleaved single-layer TMD flakes between few-nm thick hexagonal boron nitride (hBN) crystals, an insulator.[77] Encapsulation with hBN is a common procedure used to protect layered materials from electric and dielectric fluctuations of the local environment[78] and avoid sample degradation.[79-80] This leads to reduced exciton linewidth, lower electrostatic doping, and enhanced homogeneity.[78,77] To compare the optical properties of our colloidal TMDs to their state-of-the-art solid-state counterparts, our colloidal samples were also encapsulated in hBN, and photoluminescence (PL) spectra were collected at various temperatures ranging between 4 K and 295 K (**Figure 5**).

In **Figure 5,** we report the evolution of the PL spectra with temperature for both samples, as well as the associated shift in band gap and variation of the linewidth. Both samples show a progressive blue shift (*i.e.* shift toward higher energy) and line width narrowing going from 295 K to 4 K. The 4 K emission energy is consistent for large monolayers, with values of 1.96 eV for MoS_2 and 1.68

eV for $MoSe_2$, reported for neutral excitons[77-78, 81] The temperature dependence of the band gap is fitted with the O'Donnell-Chen[82] model:

$$E_g(T) = E_0 - S\langle\hbar\omega\rangle[\coth\left(\frac{\langle\hbar\omega\rangle}{2kT}\right) - 1] \quad \textbf{(2)}$$

For MoS_2 ($MoSe_2$) we obtained an E_0 of 1.96 eV (1.67 eV), an electron-phonon coupling constant S of 2.37 (2.46) and an average phonon energy $\langle\hbar\omega\rangle$ of 25 meV (17 meV). These values are in good agreement with mechanical exfoliated and CVD literature.[83-86] The excitonic linewidth of MoX_2 includes the intrinsic line width Δ_0, and a contribution from acoustic Δ_{AC} and LO Δ_{LO} phonon coupling that increases with temperature, yielding the following temperature dependence:

$$\Delta(T) = \Delta_0 + \Delta_{AC}T + \Delta_{LO}\frac{1}{e^{E_{LO}/k_BT}-1} \quad \textbf{(3)}$$

The parameter E_{LO} is the LO phonon energy (here taken as the energy of the Raman mode E^1_{2g}); this is 47.7 meV and 29.6 meV for MoS_2 and $MoSe_2$, respectively. For both fits Δ_{AC} is fixed to zero. As a result, we found that for MoS_2 $\Delta_0 = 76 \pm 2$ meV, and $\Delta_{LO} = 210 \pm 24$ meV, while for $MoSe_2$ $\Delta_0 = 38.6 \pm 0.2$ meV, and $\Delta_{LO} = 39.7 \pm 0.9$ meV. Literature reports values of Δ_0 between 52 - 66 meV for MoS_2 (4 meV in hBN-encapsulated MoS_2) and 1.5-4.3 meV for $MoSe_2$, respectively, and values of Δ_{LO} between 42.6 – 86 meV for MoS_2 and 11.2 – 15.6 meV for $MoSe_2$, respectively.[77, 87-91] This suggest that our colloidal TMD nanosheets can still be further improved however, our $MoSe_2$ monolayer already exhibits a substantially narrower emission linewidth than the MoS_2 monolayer, suggesting that the latter might be more suitable for further application in optoelectronic or photonic devices.[92-94]

CONCLUSION

Using a Design of Experiments approach, we were able to optimize the MoS_2 synthesis protocol using a minimal number of synthesis runs, and screen the main factors involved in the synthesis. The optimization has led to the synthesis of MoS_2 with A exciton absorption wavelength and a Raman mode splitting that confirms a significant monolayer yield in the samples. The protocol has been extended to the synthesis of $MoSe_2$, showing the generality of the method. The obtained $MoSe_2$ sample again shows an A exciton absorption wavelength, and Raman modes that agree with a significant monolayer yield. The samples show photoluminescence, with $MoSe_2$ clearly showing narrower emission features, thus providing a pathway toward further improvement based on the DOE approach. We expect that on longer term, this can lead to colloidal TMDs being a viable, scalable, and cost effective alternative to other TMD synthesis approaches.

EXPERIMENTAL SECTION

Materials. Molybdenum pentachloride ($MoCl_5$, 99.99%, Sigma-Aldrich), elemental sulfur (≥ 99.95%, Sigma-Aldrich) and selenium (≥ 99.99%, Strem Chemicals), 1,2-dichlorobenzene (o-DCB, 99%, Acros Organics) and chloroform are used without any purification. 1-octadecene (ODE, Sigma-Aldrich,) and oleylamine (OLA, 80-90% Acros Organics) are dried using calcium hydride, distilled and stored under nitrogen until further use.

General DOE 2H-MoS_2 Synthesis. The synthesis is performed under nitrogen using standard Schlenk line techniques. All amounts and temperatures used are mentioned in **Table 1**. As an example, in a 25 mL three-neck flask, a solution of OLA and sulfur is degassed under vacuum. After degassing, the temperature is raised and a solution of $MoCl_5$ in ODE (0.05 g in 3 mL of ODE, sonicated until complete dissolution) is injected using a syringe pump. After 1 h, the MoS_2 solution is cooled and the product is purified three times using a mixture of hexane/isopropanol, toluene/isopropanol and dichlorobenzene/isopropanol respectively, followed by centrifugation at 5000 rpm to collect the sample. The nanosheets are finally dispersed in o-DCB.

Optimized 2H-MoS_2 Nanosheet Synthesis. The synthesis is performed under nitrogen using standard Schlenk line technique. In a 25 ml three-neck flask a solution of OLA (15 mL) and sulfur (41 mg) is degassed under vacuum (120°C, 150 min). After degassing, the temperature is raised up to 300°C and a solution of $MoCl_5$ in ODE (0.017 g in 1 mL, sonicated until complete dissolution) is injected at 9 $mL \cdot h^{-1}$ using a syringe pump. After injection, 10 mL of fresh OLA from the glovebox is injected in the MoS_2 solution and a water bath is used to cool it. The product is purified as described above, and finally dispersed in o-DCB.

Optimized 2H-$MoSe_2$ Nanosheet Synthesis. The synthesis is performed under nitrogen using standard Schlenk line techniques. In a 25 ml three-neck flask, a solution of OLA (15 mL) and selenium (10 mg) is heated up to 290 °C and a solution of $MoCl_5$ in ODE (0.017 g in 1 mL, sonicated until complete dissolution) is injected at 12 $mL \cdot h^{-1}$ using a syringe pump. After the injection, the solution is cooled using a water bath. The product is purified three times using a mixture of toluene/isopropanol/acetone, hexane/isopropanol and chloroform/isopropanol respectively, followed by centrifugation at 5000 rpm to collect the sample. The nanosheets are finally dispersed in chloroform.

Characterization methods. High Resolution Transmission Electron Microscopy (HR-TEM) images were acquired on an image-Cs-corrected JEM-2200FS TEM (JEOL), operated at 200 kV. The samples were prepared by drop-casting of the suspension onto ultrathin C/holey C/Cu TEM grids. Bright-field TEM images were acquired on a JEOL JEM-1011 microscope operating at an accelerating voltage of 100 kV. The samples were prepared by drop-casting of the suspension onto ultrathin C/holey C/Cu TEM grids. Raman spectra were collected with a Bruker Optics '*Senterra*' dispersive Raman spectrometer. The spectrometer is coupled to an Olympus BX51 microscope and to a thermoelectrically cooled charge coupled device (CCD) detector, operating at −65°C. The point measurements were conducted on dried droplets on glass slides and by using the 532 nm laser of the Raman system. The experimental conditions selected were: 5 or 10 accumulations of 10 seconds, 3–5 cm^{-1} spectral resolution, 40–1540 cm^{-1} spectral range, 50 μm pinhole-type

aperture, ×50 (NA: 0.75) magnification objective (corresponding to a less than 4 μm spot size) and a 0.20 % laser power (corresponding approx. to 0.12 mW). Ultraviolet-Visible (UV-Vis) absorption spectra of MoS_2 nanosheets in o-DCB (chloroform for $MoSe_2$) were recorded using a PerkinElmer Lambda 950 spectrometer using a 1 cm path length quartz cuvette. Photoluminescence spectra were measured using a custom-made confocal microscope in backscattering geometry. The excitation laser beam is focused on the sample by an objective with numerical aperture NA = 0.75 to a diffraction-limited spot. For cryogenic measurements a He-flow cryostat (Cryovac) was used, and the emitted light was directed to a spectrometer (Horiba, 300 grooves/mm) coupled to a nitrogen-cooled CCD. XPS analyses were carried out using a Kratos Axis UltraDLD spectrometer. Data were acquired using a monochromatic Al Kα source, operated at 20 mA and 15 kV. High resolution spectra were acquired at pass energy of 20 eV, energy step of 0.1 eV and take-off angle of 0 degrees with respect to sample normal direction.

ASSOCIATED CONTENT

Supporting Information. The Supporting Information is available free of charge at [WEBLINK]. Design of Experiments, Definitive Screening Design on MoS_2: evolution of absorption spectrum of C1 and C3, absorption spectra of 60 min aliquot for all the runs, analysis of Rayleigh scattering background, and peak sharpness, XPS analysis on samples C1 and C3.

AUTHOR INFORMATION

Corresponding Author

* Iwan Moreels, Department of Chemistry, Ghent University, 9000 Ghent, Belgium.

iwan.moreels@ugent.be

Author Contributions

The manuscript was written through contributions of all authors. All authors have given approval to the final version of the manuscript.

Funding Sources

This project has received funding from the European Research Council (ERC) under the European Union's Horizon 2020 research and innovation program (grant agreement no. 714876 PHOCONA), from the European Union Horizon 2020 research and innovation programme under Grant Agreement No. 820423 (S2QUIP), and the Deutsche Forschungsgemeinschaft (DFG, German Research Foundation) under Germany's Excellence Strategy – MCQST (EXC-2111, 390814868) and e-Conversion (EXC-2089). M.B. acknowledges support from the Alexander von Humboldt Foundation. K. M. acknowledges support from the Bavarian Academy of Sciences and Humanities. A. R. greatly acknowledges the special research fund (BOF) of Ghent University, for her postdoctoral fellowship (Ghent University-BOF postdoctoral fellowship).

REFERENCES

1. Wilson, J. A.; Yoffe, A. D., The transition metal dichalcogenides discussion and interpretation of the observed optical, electrical and structural properties. *Advances in Physics* **1969,** *18* (73), 193-335.
2. Strachan, J.; Masters, A. F.; Maschmeyer, T., 3R-MoS2 in Review: History, Status, and Outlook. *ACS Applied Energy Materials* **2021,** *4* (8), 7405-7418.
3. Song, I.; Park, C.; Choi, H. C., Synthesis and properties of molybdenum disulphide: from bulk to atomic layers. *RSC Advances* **2015,** *5* (10), 7495-7514.
4. Kam, K. K.; Parkinson, B. A., Detailed photocurrent spectroscopy of the semiconducting group VIB transition metal dichalcogenides. *The Journal of Physical Chemistry* **1982,** *86* (4), 463-467.
5. Cheiwchanchamnangij, T.; Lambrecht, W. R. L., Quasiparticle band structure calculation of monolayer, bilayer, and bulk MoS2. *Physical Review B* **2012,** *85* (20), 205302.
6. Zhang, Y.; Chang, T. R.; Zhou, B.; Cui, Y. T.; Yan, H.; Liu, Z.; Schmitt, F.; Lee, J.; Moore, R.; Chen, Y.; Lin, H.; Jeng, H. T.; Mo, S. K.; Hussain, Z.; Bansil, A.; Shen, Z. X., Direct observation of the transition from indirect to direct bandgap in atomically thin epitaxial MoSe2. *Nature nanotechnology* **2014,** *9* (2), 111-5.
7. Xiao, D.; Liu, G. B.; Feng, W.; Xu, X.; Yao, W., Coupled spin and valley physics in monolayers of MoS2 and other group-VI dichalcogenides. *Physical review letters* **2012,** *108* (19), 196802.
8. Song, Z.; Quhe, R.; Liu, S.; Li, Y.; Feng, J.; Yang, Y.; Lu, J.; Yang, J., Tunable Valley Polarization and Valley Orbital Magnetic Moment Hall Effect in Honeycomb Systems with Broken Inversion Symmetry. *Scientific reports* **2015,** *5*, 13906.
9. Chen, L.; Feng, H.; Zhang, R.; Wang, S.; Zhang, X.; Wei, Z.; Zhu, Y.; Gu, M.; Zhao, C., Phase-Controlled Synthesis of 2H/3R-MoSe2 Nanosheets on P-Doped Carbon for Synergistic Hydrogen Evolution. *ACS Applied Nano Materials* **2020,** *3* (7), 6516-6523.
10. Singh, E.; Singh, P.; Kim, K. S.; Yeom, G. Y.; Nalwa, H. S., Flexible Molybdenum Disulfide (MoS2) Atomic Layers for Wearable Electronics and Optoelectronics. *ACS applied materials & interfaces* **2019,** *11* (12), 11061-11105.
11. Luo, Y. K.; Xu, J.; Zhu, T.; Wu, G.; McCormick, E. J.; Zhan, W.; Neupane, M. R.; Kawakami, R. K., Opto-Valleytronic Spin Injection in Monolayer MoS2/Few-Layer Graphene Hybrid Spin Valves. *Nano letters* **2017,** *17* (6), 3877-3883.
12. Liu, Y.; Gao, Y.; Zhang, S.; He, J.; Yu, J.; Liu, Z., Valleytronics in transition metal dichalcogenides materials. *Nano Research* **2019,** *12* (11), 2695-2711.
13. Cheng, L.; Huang, W.; Gong, Q.; Liu, C.; Liu, Z.; Li, Y.; Dai, H., Ultrathin WS2 nanoflakes as a high-performance electrocatalyst for the hydrogen evolution reaction. *Angewandte Chemie* **2014,** *53* (30), 7860-3.
14. Guo, X.; Hou, Y.; Ren, R.; Chen, J., Temperature-dependent Crystallization of MoS2 Nanoflakes on Graphene Nanosheets for Electrocatalysis. *Nanoscale research letters* **2017,** *12* (1), 479.
15. Pu, J.; Yomogida, Y.; Liu, K. K.; Li, L. J.; Iwasa, Y.; Takenobu, T., Highly flexible MoS2 thin-film transistors with ion gel dielectrics. *Nano letters* **2012,** *12* (8), 4013-7.
16. Novoselov, K. S.; Geim, A. K.; Morozov, S. V.; Jiang, D.; Zhang, Y.; Dubonos, S. V.; Grigorieva, I. V.; Firsov, A. A., Electric field effect in atomically thin carbon films. *Science* **2004,** *306* (5696), 666-9.

17. Tao, H.; Zhang, Y.; Gao, Y.; Sun, Z.; Yan, C.; Texter, J., Scalable exfoliation and dispersion of two-dimensional materials - an update. *Physical chemistry chemical physics : PCCP* **2017,** *19* (2), 921-960.
18. Lin, Z.; Liu, Y.; Halim, U.; Ding, M.; Liu, Y.; Wang, Y.; Jia, C.; Chen, P.; Duan, X.; Wang, C.; Song, F.; Li, M.; Wan, C.; Huang, Y.; Duan, X., Solution-processable 2D semiconductors for high-performance large-area electronics. *Nature* **2018,** *562* (7726), 254-258.
19. Castellanos-Gomez, A.; Barkelid, M.; Goossens, A. M.; Calado, V. E.; van der Zant, H. S.; Steele, G. A., Laser-thinning of MoS(2): on demand generation of a single-layer semiconductor. *Nano letters* **2012,** *12* (6), 3187-92.
20. Samadi, M.; Sarikhani, N.; Zirak, M.; Zhang, H.; Zhang, H.-L.; Moshfegh, A. Z., Group 6 transition metal dichalcogenide nanomaterials: synthesis, applications and future perspectives. *Nanoscale Horizons* **2018,** *3* (2), 90-204.
21. Jung, W.; Lee, S.; Yoo, D.; Jeong, S.; Miro, P.; Kuc, A.; Heine, T.; Cheon, J., Colloidal synthesis of single-layer MSe2 (M = Mo, W) nanosheets via anisotropic solution-phase growth approach. *Journal of the American Chemical Society* **2015,** *137* (23), 7266-9.
22. Pang, Y.; Uddin, M. N.; Chen, W.; Javaid, S.; Barker, E.; Li, Y.; Suvorova, A.; Saunders, M.; Yin, Z.; Jia, G., Colloidal Single-Layer Photocatalysts for Methanol-Storable Solar H2 Fuel. *Advanced materials* **2019,** *31* (49), e1905540.
23. Li, X.; Tang, A.; Li, J.; Guan, L.; Dong, G.; Teng, F., Heating-up Synthesis of MoS2 Nanosheets and Their Electrical Bistability Performance. *Nanoscale research letters* **2016,** *11* (1), 171.
24. Sun, Y.; Alimohammadi, F.; Zhang, D.; Guo, G., Enabling Colloidal Synthesis of Edge-Oriented MoS2 with Expanded Interlayer Spacing for Enhanced HER Catalysis. *Nano letters* **2017,** *17* (3), 1963-1969.
25. Sun, D.; Feng, S.; Terrones, M.; Schaak, R. E., Formation and Interlayer Decoupling of Colloidal MoSe2Nanoflowers. *Chemistry of Materials* **2015,** *27* (8), 3167-3175.
26. Lin, Z.; McCreary, A.; Briggs, N.; Subramanian, S.; Zhang, K. H.; Sun, Y. F.; Li, X. F.; Borys, N. J.; Yuan, H. T.; Fullerton-Shirey, S. K.; Chernikov, A.; Zhao, H.; McDonnell, S.; Lindenberg, A. M.; Xiao, K.; LeRoy, B. J.; Drndic, M.; Hwang, J. C. M.; Park, J.; Chhowalla, M.; Schaak, R. E.; Javey, A.; Hersam, M. C.; Robinson, J.; Terrones, M., 2D materials advances: from large scale synthesis and controlled heterostructures to improved characterization techniques, defects and applications. *2d Materials* **2016,** *3* (4), 022002.
27. Son, D.; Chae, S. I.; Kim, M.; Choi, M. K.; Yang, J.; Park, K.; Kale, V. S.; Koo, J. H.; Choi, C.; Lee, M.; Kim, J. H.; Hyeon, T.; Kim, D. H., Colloidal Synthesis of Uniform-Sized Molybdenum Disulfide Nanosheets for Wafer-Scale Flexible Nonvolatile Memory. *Advanced materials* **2016,** *28* (42), 9326-9332.
28. Aabid, A.; Khan, S. A., Investigation of High-Speed Flow Control from CD Nozzle Using Design of Experiments and CFD Methods. *Arabian Journal for Science and Engineering* **2020,** *46* (3), 2201-2230.
29. Gilman, J.; Walls, L.; Bandiera, L.; Menolascina, F., Statistical Design of Experiments for Synthetic Biology. *ACS synthetic biology* **2021,** *10* (1), 1-18.
30. Bowden, G. D.; Pichler, B. J.; Maurer, A., A Design of Experiments (DoE) Approach Accelerates the Optimization of Copper-Mediated (18)F-Fluorination Reactions of Arylstannanes. *Scientific reports* **2019,** *9* (1), 11370.
31. Leardi, R., Experimental design in chemistry: A tutorial. *Analytica chimica acta* **2009,** *652* (1-2), 161-72.

32. Varrla, E.; Backes, C.; Paton, K. R.; Harvey, A.; Gholamvand, Z.; McCauley, J.; Coleman, J. N., Large-Scale Production of Size-Controlled MoS2 Nanosheets by Shear Exfoliation. *Chemistry of Materials* **2015,** *27* (3), 1129-1139.
33. Liu, H.; Xu, L.; Liu, W.; Zhou, B.; Zhu, Y.; Zhu, L.; Jiang, X., Production of mono- to few-layer MoS2 nanosheets in isopropanol by a salt-assisted direct liquid-phase exfoliation method. *Journal of colloid and interface science* **2018,** *515*, 27-31.
34. Mourdikoudis, S.; Liz-Marzán, L. M., Oleylamine in Nanoparticle Synthesis. *Chemistry of Materials* **2013,** *25* (9), 1465-1476.
35. Altavilla, C.; Sarno, M.; Ciambelli, P., A Novel Wet Chemistry Approach for the Synthesis of Hybrid 2D Free-Floating Single or Multilayer Nanosheets of MS2@oleylamine (M═Mo, W). *Chemistry of Materials* **2011,** *23* (17), 3879-3885.
36. Savjani, N.; Lewis, E. A.; Bissett, M. A.; Brent, J. R.; Dryfe, R. A. W.; Haigh, S. J.; O'Brien, P., Synthesis of Lateral Size-Controlled Monolayer 1H-MoS2@Oleylamine as Supercapacitor Electrodes. *Chemistry of Materials* **2016,** *28* (2), 657-664.
37. Thomson, J. W.; Nagashima, K.; Macdonald, P. M.; Ozin, G. A., From sulfur-amine solutions to metal sulfide nanocrystals: peering into the oleylamine-sulfur black box. *Journal of the American Chemical Society* **2011,** *133* (13), 5036-41.
38. Zimdars, J.; Bredol, M., On the influence of coordinating solvents on the reduction of selenium for the phosphine-free synthesis of metal selenide nanoparticles. *New Journal of Chemistry* **2016,** *40* (2), 1137-1142.
39. Guo, Y.; Sun, D.; Ouyang, B.; Raja, A.; Song, J.; Heinz, T. F.; Brus, L. E., Probing the Dynamics of the Metallic-to-Semiconducting Structural Phase Transformation in MoS2 Crystals. *Nano letters* **2015,** *15* (8), 5081-8.
40. Eda, G.; Yamaguchi, H.; Voiry, D.; Fujita, T.; Chen, M.; Chhowalla, M., Photoluminescence from chemically exfoliated MoS2. *Nano letters* **2011,** *11* (12), 5111-6.
41. Chou, S. S.; Huang, Y. K.; Kim, J.; Kaehr, B.; Foley, B. M.; Lu, P.; Dykstra, C.; Hopkins, P. E.; Brinker, C. J.; Huang, J.; Dravid, V. P., Controlling the metal to semiconductor transition of MoS2 and WS2 in solution. *Journal of the American Chemical Society* **2015,** *137* (5), 1742-5.
42. Jones, B.; Nachtsheim, C. J., A Class of Three-Level Designs for Definitive Screening in the Presence of Second-Order Effects. *Journal of Quality Technology* **2017,** *43* (1), 1-15.
43. Santos, C. P.; Rato, T. J.; Reis, M. S., Design of Experiments: A comparison study from the non-expert user's perspective. *Journal of Chemometrics* **2019,** *33* (1), e3087.
44. Xiao, L.; Lin, D. K. J.; Bai, F., Constructing Definitive Screening Designs Using Conference Matrices. *Journal of Quality Technology* **2017,** *44* (1), 2-8.
45. Boles, M. A.; Ling, D.; Hyeon, T.; Talapin, D. V., The surface science of nanocrystals. *Nature materials* **2016,** *15* (3), 364.
46. Wang, L.; Wang, Z.; Wang, H. Y.; Grinblat, G.; Huang, Y. L.; Wang, D.; Ye, X. H.; Li, X. B.; Bao, Q.; Wee, A. S.; Maier, S. A.; Chen, Q. D.; Zhong, M. L.; Qiu, C. W.; Sun, H. B., Slow cooling and efficient extraction of C-exciton hot carriers in MoS2 monolayer. *Nature communications* **2017,** *8*, 13906.
47. Synnatschke, K.; Cieslik, P. A.; Harvey, A.; Castellanos-Gomez, A.; Tian, T.; Shih, C.-J.; Chernikov, A.; Santos, E. J. G.; Coleman, J. N.; Backes, C., Length- and Thickness-Dependent Optical Response of Liquid-Exfoliated Transition Metal Dichalcogenides. *Chemistry of Materials* **2019,** *31* (24), 10049-10062.

48. Jayabal, S.; Wu, J.; Chen, J.; Geng, D.; Meng, X., Metallic 1T-MoS2 nanosheets and their composite materials: Preparation, properties and emerging applications. *Materials Today Energy* **2018,** *10*, 264-279.
49. Niu, Y.; Gonzalez-Abad, S.; Frisenda, R.; Marauhn, P.; Druppel, M.; Gant, P.; Schmidt, R.; Taghavi, N. S.; Barcons, D.; Molina-Mendoza, A. J.; de Vasconcellos, S. M.; Bratschitsch, R.; Perez De Lara, D.; Rohlfing, M.; Castellanos-Gomez, A., Thickness-Dependent Differential Reflectance Spectra of Monolayer and Few-Layer MoS(2), MoSe(2), WS(2) and WSe(2). *Nanomaterials* **2018,** *8* (9), 725.
50. Jin, W.; Yeh, P. C.; Zaki, N.; Zhang, D.; Sadowski, J. T.; Al-Mahboob, A.; van der Zande, A. M.; Chenet, D. A.; Dadap, J. I.; Herman, I. P.; Sutter, P.; Hone, J.; Osgood, R. M., Jr., Direct measurement of the thickness-dependent electronic band structure of MoS2 using angle-resolved photoemission spectroscopy. *Physical review letters* **2013,** *111* (10), 106801.
51. O'Neill, A.; Khan, U.; Coleman, J. N., Preparation of High Concentration Dispersions of Exfoliated MoS2 with Increased Flake Size. *Chemistry of Materials* **2012,** *24* (12), 2414-2421.
52. Jawaid, A.; Nepal, D.; Park, K.; Jespersen, M.; Qualley, A.; Mirau, P.; Drummy, L. F.; Vaia, R. A., Mechanism for Liquid Phase Exfoliation of MoS2. *Chemistry of Materials* **2015,** *28* (1), 337-348.
53. Backes, C.; Smith, R. J.; McEvoy, N.; Berner, N. C.; McCloskey, D.; Nerl, H. C.; O'Neill, A.; King, P. J.; Higgins, T.; Hanlon, D.; Scheuschner, N.; Maultzsch, J.; Houben, L.; Duesberg, G. S.; Donegan, J. F.; Nicolosi, V.; Coleman, J. N., Edge and confinement effects allow in situ measurement of size and thickness of liquid-exfoliated nanosheets. *Nature communications* **2014,** *5*, 4576.
54. Muscuso, L.; Cravanzola, S.; Cesano, F.; Scarano, D.; Zecchina, A., Optical, Vibrational, and Structural Properties of MoS2Nanoparticles Obtained by Exfoliation and Fragmentation via Ultrasound Cavitation in Isopropyl Alcohol. *The Journal of Physical Chemistry C* **2015,** *119* (7), 3791-3801.
55. Lee, C.; Yan, H.; Brus, L. E.; Heinz, T. F.; Hone, J.; Ryu, S., Anomalous lattice vibrations of single- and few-layer MoS2. *ACS nano* **2010,** *4* (5), 2695-700.
56. Sahoo, S.; Gaur, A. P. S.; Ahmadi, M.; Guinel, M. J. F.; Katiyar, R. S., Temperature-Dependent Raman Studies and Thermal Conductivity of Few-Layer MoS2. *The Journal of Physical Chemistry C* **2013,** *117* (17), 9042-9047.
57. Mignuzzi, S.; Pollard, A. J.; Bonini, N.; Brennan, B.; Gilmore, I. S.; Pimenta, M. A.; Richards, D.; Roy, D., Effect of disorder on Raman scattering of single-layerMoS2. *Physical Review B* **2015,** *91* (19), 195411.
58. Dieterle, M.; Mestl, G., Raman spectroscopy of molybdenum oxides. *Physical Chemistry Chemical Physics* **2002,** *4* (5), 822-826.
59. Li, H.; Zhang, Q.; Yap, C. C. R.; Tay, B. K.; Edwin, T. H. T.; Olivier, A.; Baillargeat, D., From Bulk to Monolayer MoS2: Evolution of Raman Scattering. *Advanced Functional Materials* **2012,** *22* (7), 1385-1390.
60. Jeon, J.; Jang, S. K.; Jeon, S. M.; Yoo, G.; Jang, Y. H.; Park, J. H.; Lee, S., Layer-controlled CVD growth of large-area two-dimensional MoS2 films. *Nanoscale* **2015,** *7* (5), 1688-95.
61. Özden, A.; Şar, H.; Yeltik, A.; Madenoğlu, B.; Sevik, C.; Ay, F.; Perkgöz, N. K., CVD grown 2D MoS2layers: A photoluminescence and fluorescence lifetime imaging study. *physica status solidi (RRL) - Rapid Research Letters* **2016,** *10* (11), 792-796.

62. Dhakal, K. P.; Duong, D. L.; Lee, J.; Nam, H.; Kim, M.; Kan, M.; Lee, Y. H.; Kim, J., Confocal absorption spectral imaging of MoS2: optical transitions depending on the atomic thickness of intrinsic and chemically doped MoS2. *Nanoscale* **2014,** *6* (21), 13028-35.
63. Ganatra, R.; Zhang, Q., Few-layer MoS2: a promising layered semiconductor. *ACS nano* **2014,** *8* (5), 4074-99.
64. Lu, X.; Utama, M. I.; Lin, J.; Gong, X.; Zhang, J.; Zhao, Y.; Pantelides, S. T.; Wang, J.; Dong, Z.; Liu, Z.; Zhou, W.; Xiong, Q., Large-area synthesis of monolayer and few-layer MoSe2 films on SiO2 substrates. *Nano letters* **2014,** *14* (5), 2419-25.
65. Zhao, Y.; Lee, H.; Choi, W.; Fei, W.; Lee, C. J., Large-area synthesis of monolayer MoSe2 films on SiO2/Si substrates by atmospheric pressure chemical vapor deposition. *RSC Advances* **2017,** *7* (45), 27969-27973.
66. Tongay, S.; Zhou, J.; Ataca, C.; Lo, K.; Matthews, T. S.; Li, J.; Grossman, J. C.; Wu, J., Thermally driven crossover from indirect toward direct bandgap in 2D semiconductors: MoSe2 versus MoS2. *Nano letters* **2012,** *12* (11), 5576-80.
67. Splendiani, A.; Sun, L.; Zhang, Y.; Li, T.; Kim, J.; Chim, C. Y.; Galli, G.; Wang, F., Emerging photoluminescence in monolayer MoS2. *Nano letters* **2010,** *10* (4), 1271-5.
68. Tai, G.; Zeng, T.; Yu, J.; Zhou, J.; You, Y.; Wang, X.; Wu, H.; Sun, X.; Hu, T.; Guo, W., Fast and large-area growth of uniform MoS2 monolayers on molybdenum foils. *Nanoscale* **2016,** *8* (4), 2234-41.
69. Backes, C.; Szydlowska, B. M.; Harvey, A.; Yuan, S.; Vega-Mayoral, V.; Davies, B. R.; Zhao, P. L.; Hanlon, D.; Santos, E. J.; Katsnelson, M. I.; Blau, W. J.; Gadermaier, C.; Coleman, J. N., Production of Highly Monolayer Enriched Dispersions of Liquid-Exfoliated Nanosheets by Liquid Cascade Centrifugation. *ACS nano* **2016,** *10* (1), 1589-601.
70. Park, M. J.; Gravelsins, S.; Son, J.; van der Zande, A. M.; Dhirani, A. A., A Scalable, Solution-Based Approach to Tuning the Solubility and Improving the Photoluminescence of Chemically Exfoliated MoS2. *ACS nano* **2019,** *13* (6), 6469-6476.
71. Frauendorf, A. P.; Niebur, A.; Harms, L.; Shree, S.; Urbaszek, B.; Oestreich, M.; Hübner, J.; Lauth, J., Room Temperature Micro-Photoluminescence Studies of Colloidal WS2 Nanosheets. *The Journal of Physical Chemistry C* **2021,** *125* (34), 18841-18848.
72. Mastria, R.; Loiudice, A.; Vávra, J.; Nobile, C.; Scarfiello, R.; Cozzoli, P. D.; Kovtun, A.; Liscio, A.; Sestu, N.; Marongiu, D.; Quochi, F.; Buonsanti, R.; Saba, M.; Calzolari, A.; Rizzo, A., Photoluminescence emission induced by localized states in halide-passivated colloidal two-dimensional WS2 nanoflakes. *Journal of Materials Chemistry C* **2021,** *9* (7), 2398-2407.
73. Mukherjee, S.; Maiti, R.; Katiyar, A. K.; Das, S.; Ray, S. K., Novel Colloidal MoS2 Quantum Dot Heterojunctions on Silicon Platforms for Multifunctional Optoelectronic Devices. *Scientific reports* **2016,** *6*, 29016.
74. Jin, H.; Ahn, M.; Jeong, S.; Han, J. H.; Yoo, D.; Son, D. H.; Cheon, J., Colloidal Single-Layer Quantum Dots with Lateral Confinement Effects on 2D Exciton. *Journal of the American Chemical Society* **2016,** *138* (40), 13253-13259.
75. Yin, W. X.; Bai, X.; Zhang, X. Y.; Zhang, J.; Gao, X. P.; Yu, W. W., Multicolor Light-Emitting Diodes with MoS2 Quantum Dots. *Particle & Particle Systems Characterization* **2019,** *36* (2), 1800362.
76. Jin, H.; Baek, B.; Kim, D.; Wu, F.; Batteas, J. D.; Cheon, J.; Son, D. H., Effects of Direct Solvent-Quantum Dot Interaction on the Optical Properties of Colloidal Monolayer WS2 Quantum Dots. *Nano letters* **2017,** *17* (12), 7471-7477.

77. Cadiz, F.; Courtade, E.; Robert, C.; Wang, G.; Shen, Y.; Cai, H.; Taniguchi, T.; Watanabe, K.; Carrere, H.; Lagarde, D.; Manca, M.; Amand, T.; Renucci, P.; Tongay, S.; Marie, X.; Urbaszek, B., Excitonic Linewidth Approaching the Homogeneous Limit in MoS2-Based van der Waals Heterostructures. *Physical Review X* **2017,** *7* (2), 021026.
78. Wierzbowski, J.; Klein, J.; Sigger, F.; Straubinger, C.; Kremser, M.; Taniguchi, T.; Watanabe, K.; Wurstbauer, U.; Holleitner, A. W.; Kaniber, M.; Muller, K.; Finley, J. J., Direct exciton emission from atomically thin transition metal dichalcogenide heterostructures near the lifetime limit. *Scientific reports* **2017,** *7* (1), 12383.
79. Cui, X.; Lee, G. H.; Kim, Y. D.; Arefe, G.; Huang, P. Y.; Lee, C. H.; Chenet, D. A.; Zhang, X.; Wang, L.; Ye, F.; Pizzocchero, F.; Jessen, B. S.; Watanabe, K.; Taniguchi, T.; Muller, D. A.; Low, T.; Kim, P.; Hone, J., Multi-terminal transport measurements of MoS2 using a van der Waals heterostructure device platform. *Nature nanotechnology* **2015,** *10* (6), 534-40.
80. Vandana, S.; Kochat, V.; Lee, J.; Varshney, V.; Yazdi, S.; Shen, J.; Kosolwattana, S.; Vinod, S.; Vajtai, R.; Roy, A. K.; Tiwary, C. S.; Ajayan, P. M., 2D Heterostructure coatings ofhBN-MoS2layers for corrosion resistance. *Journal of Physics D: Applied Physics* **2017,** *50* (4), 045301.
81. Arora, A.; Wessling, N. K.; Deilmann, T.; Reichenauer, T.; Steeger, P.; Kossacki, P.; Potemski, M.; de Vasconcellos, S. M.; Rohlfing, M.; Bratschitsch, R., Dark trions govern the temperature-dependent optical absorption and emission of doped atomically thin semiconductors. *Physical Review B* **2020,** *101* (24), 241413.
82. O'Donnell, K. P.; Chen, X., Temperature dependence of semiconductor band gaps. *Applied Physics Letters* **1991,** *58* (25), 2924-2926.
83. Pei, J.; Yang, J.; Xu, R.; Zeng, Y. H.; Myint, Y. W.; Zhang, S.; Zheng, J. C.; Qin, Q.; Wang, X.; Jiang, W.; Lu, Y., Exciton and Trion Dynamics in Bilayer MoS2. *Small* **2015,** *11* (48), 6384-90.
84. Arora, A.; Nogajewski, K.; Molas, M.; Koperski, M.; Potemski, M., Exciton band structure in layered MoSe2: from a monolayer to the bulk limit. *Nanoscale* **2015,** *7* (48), 20769-75.
85. Ko, T. S.; Huang, C. C.; Lin, D. Y., Optical and Transport Properties of Ni-MoS2. *Appl Sci-Basel* **2016,** *6* (8).
86. Christopher, J. W.; Goldberg, B. B.; Swan, A. K., Long tailed trions in monolayer MoS2: Temperature dependent asymmetry and resulting red-shift of trion photoluminescence spectra. *Scientific reports* **2017,** *7* (1), 14062.
87. Dey, P.; Paul, J.; Wang, Z.; Stevens, C. E.; Liu, C.; Romero, A. H.; Shan, J.; Hilton, D. J.; Karaiskaj, D., Optical Coherence in Atomic-Monolayer Transition-Metal Dichalcogenides Limited by Electron-Phonon Interactions. *Physical review letters* **2016,** *116* (12), 127402.
88. Kumar, D.; Kumar, R.; Kumar, M.; Kumar, P., Coupled excitonic quasiparticle-electron–phonon and interlayer coupling in vertically and horizontally aligned MoS2. *Journal of Materials Chemistry C* **2022,** *10* (14), 5684-5692.
89. Wei, G.; Czaplewski, D. A.; Lenferink, E. J.; Stanev, T. K.; Jung, I. W.; Stern, N. P., Size-tunable Lateral Confinement in Monolayer Semiconductors. *Scientific reports* **2017,** *7* (1), 3324.
90. Shree, S.; Semina, M.; Robert, C.; Han, B.; Amand, T.; Balocchi, A.; Manca, M.; Courtade, E.; Marie, X.; Taniguchi, T.; Watanabe, K.; Glazov, M. M.; Urbaszek, B., Observation of exciton-phonon coupling in MoSe2 monolayers. *Physical Review B* **2018,** *98* (3).
91. Selig, M.; Berghauser, G.; Raja, A.; Nagler, P.; Schuller, C.; Heinz, T. F.; Korn, T.; Chernikov, A.; Malic, E.; Knorr, A., Excitonic linewidth and coherence lifetime in monolayer transition metal dichalcogenides. *Nature communications* **2016,** *7*, 13279.

92. Ghorai, A.; Ray, S. K.; Midya, A., MoSe2 Nanosheets with Tuneable Optical Properties for Broadband Visible Light Photodetection. *ACS Applied Nano Materials* **2021,** *4* (3), 2999-3006.
93. Tulsani, S. R.; Rath, A. K.; Late, D. J., 2D-MoS2 nanosheets as effective hole transport materials for colloidal PbS quantum dot solar cells. *Nanoscale Advances* **2019,** *1* (4), 1387-1394.
94. Sahoo, D.; Shakya, J.; Ali, N.; Yoo, W. J.; Kaviraj, B., Edge Rich Ultrathin Layered MoS2 Nanostructures for Superior Visible Light Photocatalytic Activity. *Langmuir : the ACS journal of surfaces and colloids* **2022,** *38* (4), 1578-1588.